

# Classification of the reversible-irreversible transitions in particle trajectories across the jamming transition point

Kentaro Nagasawa,<sup>1,2</sup> Kunimasa Miyazaki,<sup>1</sup> and Takeshi Kawasaki<sup>1</sup>

<sup>1</sup>*Department of Physics, Nagoya University, Nagoya 464-8602, Japan*

<sup>2</sup>*Department of Physics, The University of Tokyo, Bunkyo-ku, Tokyo 113-0033, Japan*

(Dated: October 14, 2019)

The reversible-irreversible (RI) transition of particle trajectories in athermal colloidal suspensions under cyclic shear deformation is an archetypal nonequilibrium phase transition which attracts much attention recently. Most studies of the RI transitions have focused on either dilute limit or very high densities well above the jamming transition point. The transition between the two limiting cases is largely unexplored. In this paper, we study the RI transition of athermal frictionless colloidal particles over a wide range of densities, with emphasis on the region below  $\varphi_J$ , by using oscillatory sheared molecular dynamics simulation. We reveal that the nature of the RI transitions in the intermediate densities is very rich. As demonstrated by the previous work by Schreck *et al.* [Phys. Rev. E. **88**, 052205 (2013)], there exist the point-reversible and the loop-reversible phases depending on the density and the shear strain amplitude. We find that, between the two reversible phases, a quasi-irreversible phase where the particles' trajectories are highly non-affine and diffusive. The averaged number of contacts of particles is found to characterize the phase boundaries. We also find that the system undergoes the yielding transition below but in the vicinity of  $\varphi_J$  when the strain with a small but finite strain rate is applied. This yielding transition line matches with the RI transition line separating the loop-reversible from the irreversible phases. Surprisingly, the nonlinear rheological response called “softening” has been observed even below  $\varphi_J$ . These findings imply that geometrical properties encoded in the sheared configurations control the dynamical transitions.

PACS numbers: 05.10.-a,61.43.-j,83.50.-v

## I. INTRODUCTION

Athermal colloidal suspensions driven by cyclic shear are the simplest model system to study mechanical, rheological, and flow properties of the complex fluids. Recently, there have been many attempts to connect these macroscopic behaviors with the microscopic reversibility of trajectories of constituting particles. If the amplitude of the oscillatory shear strain is small, the system finds an optimal configuration after many cycles and the particles return to their original positions after every cycle (or several cycles), whereas beyond a critical amplitude, the trajectories become diffusive and irreversible. This transition is referred to as the reversible-irreversible (RI) transition [1, 2].

The RI transition has been studied mainly in two different arenas: in the low density and high-density limit. In the low-density limit, the transition from the reversible to irreversible states is triggered by the instability of the trajectories due to the particle collisions and hydrodynamic interactions when the strain amplitude exceeds a critical value [3, 4]. This transition is not the chaos transition but instead is a critical phenomenon [3–6]. It is one of the nonequilibrium phase transitions in which the order parameters, relaxation time, and the correlation lengths obey power laws whose exponents are very close to those of the Directed Percolation (DP) universality class of the absorbing state transitions. Now the RI transition becomes an epitome of the nonequilibrium phase transition, along with other diverse examples, such as contact processes [1, 2], a topological transition of the

liquid crystal turbulence [7], the sheared-vortex in a superconductor [8], the skyrmions in chiral magnets [9], and the laminar-to-turbulent transition in simple fluids [10].

If the particles are soft, the RI transition also takes place at the very high density region well above the jamming transition density  $\varphi_J$ , where most particles are in contact with each other [11–19]. Even though the particles experience multiple collisions during one oscillatory cycle and the trajectories are complicated, there exists a reversible phase before the system enters to the irreversible phase at larger strain amplitudes [11, 12, 18]. Contrary to the low-density limit, this RI transition is discontinuous [20–22]; across the critical strain amplitude, the order parameter such as the number of the irreversible particles becomes finite discontinuously. Furthermore, the critical amplitude of the RI transition is almost identical to that of the yielding transition, another nonequilibrium phase transition from the elastic amorphous phase to the plastic and flowing phase.

Although the two limiting cases of low- and high-densities are relatively well investigated, attempts to bridge seamlessly the two regimes are relatively few. Most challenging is the vicinity of the jamming transition point,  $\varphi_J$ , where the three distinct transitions of the jamming, yielding, and the RI transitions meet [23, 24]. Even less explored is the intermediate density region between the low-density limit and  $\varphi_J$ . Recently, Schreck *et al.* have studied the RI transition for a broad range of densities and strains below  $\varphi_J$  [12]. They found three distinct phases, *i.e.*, the irreversible phase slightly below  $\varphi_J$ , the point-reversible phase at low strain amplitudes,

where the particles do not collide during the oscillatory cycles, and the loop-reversible state between the point-reversible and irreversible phases, where the trajectories are highly non-affine but still most of the particles reversibly come back to the original position after every (or several) cycle(s). On the other hand, the relationship between the rheological properties and the particle configurations slightly below  $\varphi_J$  is investigated by Vinutha *et al.* [25, 26], who found that the stationary configurations of the frictionless particles under quasistatic uniform shear are analogous to those of the shear-jammed frictional particles. These results suggest that the nature of the RI transition at the intermediate density region is very rich and can not be described as a mere extrapolation from the low-density region. Related results in three dimensions are presented in [27].

In this paper, we perform simulations for a two-dimensional harmonic potential system under oscillatory shear strain for a wide range of densities near the jamming transition point. We find varieties of nonequilibrium phase transitions. At the low-density side  $\varphi < \varphi_J$ , the RI transition falls into neither the DP-like continuous transition nor the discontinuous transition. We investigate the close relationship of the RI transition with both the mechanical and rheological properties on the one hand and the geometrical proprieties of the particle configurations such as the contact networks on the other hand. We examine the oscillatory strain with both zero (or quasi-static limit) and finite-frequencies. It is found that the onset of the RI transition is insensitive to the frequencies, whereas mechanical properties appreciably change with frequencies. The RI transition at the high-density side  $\varphi > \varphi_J$  is discontinuous but the one-cycle displacement of the particles which plays a role as the order parameter vanishes as the system approaches  $\varphi_J$  from above. As the density decreases further, the discontinuous RI transition line continues even below  $\varphi_J$  while the yielding transition line terminates at  $\varphi_J$ . Interestingly, when the small but finite frequency cyclic shear is applied, the yielding transition is observed even below  $\varphi_J$  and exactly at the RI transition point. We deliberately avoid studying the system exactly at  $\varphi_J$ , where the jamming criticality intervenes and analysis becomes extremely challenging.

The paper is organized as follows. We explain the simulation methods in Section II. In Section III, the order parameter of the RI transition for several densities is analyzed and we construct the nonequilibrium phase diagram. We also discuss the relationship of the phase diagram with the geometrical properties of particle trajectories and rheology of the system. Finally, we summarize and give some remarks in Section IV.

## II. SIMULATION METHOD

The system we study is a two-dimensional equimolar binary mixture of frictionless particles with diameters

$\sigma_L$  and  $\sigma_S$ , interacting with a harmonic potential. The size ratio of small and large particles is  $\sigma_L/\sigma_S = 1.4$ . We investigate the systems for a wide range of densities  $0.70 \leq \varphi \leq 1.0$ . The jamming transition density in our system is  $\varphi_J \approx 0.842$  [28]. We use the two protocols to simulate the system. The first is the finite-frequency oscillatory shear protocol, where the particles are driven by the overdamped equation with the Stokes' drag [29, 30]. The equation of motion is given by

$$\zeta_s \left[ \frac{d\mathbf{r}_i}{dt} - \dot{\gamma}(t)y_i(t)\mathbf{e}_x \right] + \sum_j \frac{\partial U(r_{ij})}{\partial \mathbf{r}_i} = 0, \quad (1)$$

where  $\zeta_s$  is a friction constant,  $r_{ij} = |\mathbf{r}_i - \mathbf{r}_j|$  is the interparticle distance between the  $i$ -th and  $j$ -th particles,  $\mathbf{e}_x = (1, 0)$  is the direction of the shear, and  $\dot{\gamma}(t)$  is the shear rate. The interaction potential is given by  $U(r_{ij}) = \frac{\epsilon}{2} (1 - r_{ij}/\sigma_{ij})^2 \Theta(\sigma_{ij} - r_{ij})$ , where  $\epsilon$  is an energy scale,  $\sigma_{ij} = (\sigma_i + \sigma_j)/2$  is the interparticle distance at contact, and  $\Theta(x)$  is the Heaviside step function. In our simulations, we use  $\sigma_S$ ,  $\tau_0 = \sigma_S^2 \zeta_s / \epsilon$ ,  $\epsilon$ , and  $\epsilon/\sigma_S^3$  as the unit of the length, time, energy, and the stress, respectively. We apply an oscillatory deformation using the Lees-Edwards periodic boundary condition [30]. The time evolution of the strain is given by  $\gamma(t) = \gamma_0 [1 - \cos(\omega t)]$ , where  $\gamma_0$  is the amplitude of the imposed shear strain and  $\omega = 2\pi/T$  is the frequency of the oscillation. We compute an initial configuration as a random distribution at  $t = 0$ . The oscillation period  $T$  is chosen to be very large and we use mainly  $T = 10^4 \tau_0$ . We solve Eq. (1) discretized with the semi-implicit Euler's algorithm. The time-step is chosen to be  $\Delta t = 0.1$ . We have checked that using the higher order discretization algorithm such as the Heun method does not alter the results [30], because our simulations are driven slowly enough with the overdamped equations of motion and the accumulation of the rounding-off error is suppressed. We also note that the velocity Verlet method, which is used in a micro-canonical molecular dynamics simulations, is not applicable in our simulations, because our system is fully overdamped. The system size is  $L = 20$  for the results presented in the main text. We confirm that the main results do not qualitatively change with the larger system size of  $L = 40$ . The maximal simulation time is set to  $t_{\text{sim}} = 4000T$ . To improve the statistics, we perform at least five independent runs in each of the parameter sets of  $(\varphi, \gamma_0)$ . We use the bracketing symbol  $\langle \dots \rangle$  for ensemble averages of variables discussed below.

The second is the athermal quasi-static (AQS) protocol which corresponds to the small strain rate limit  $\dot{\gamma} \rightarrow 0$ . We first give the small shear strain at each step to drive the particles toward the shear direction by

$$\mathbf{r}'_j(n+1) = \mathbf{r}_j(n) + \Delta\gamma(n)y_j(n)\mathbf{e}_x, \quad (2)$$

where  $\mathbf{r}_j(n)$  is the position of the  $j$ -th particle at the  $n$ -th simulation step. After one step, the position of the particles,  $\mathbf{r}'_j(n+1)$ , are relaxed by the conjugate gradient line-search algorithm to minimize the energy.

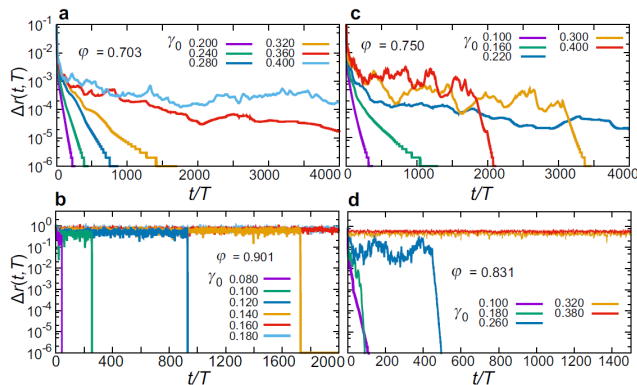


FIG. 1. The time evolution of the averaged one-cycle displacement  $\Delta r(t, T)$ . (a): At  $\varphi = 0.703$  far below  $\varphi_J$ . For  $\gamma_0 \lesssim 0.40$ ,  $\Delta r(t, T)$  continuously drop to zero after a timescale  $\tau_L$  (see the main text for the definition of  $\tau_L$ ). (b): At  $\varphi = 0.901$  far above  $\varphi_J$ . For  $\gamma_0 \lesssim 0.14$ ,  $\Delta r(t, T)$  discontinuously drop to zero. (c): At  $\varphi = 0.750$ . For small  $\gamma_0 (\gtrsim 0.2)$ ,  $\Delta r(t, T)$  relaxes to zero exponentially with a power law tail, whereas, for  $\gamma_0 \sim 0.2$ ,  $\Delta r(t, T)$  first relaxes to a finite value before it discontinuously drop to zero. (d): At  $\varphi = 0.831$  slightly below  $\varphi_J$ . For  $\gamma_0 \lesssim 0.30$ , the displacements semi-discontinuously drop to zero.

The shear strain evolves with  $\gamma(n+1) = \gamma(n) + \Delta\gamma(n)$ , where  $\Delta\gamma(n) = 2\gamma_0\pi/N_{\text{cycle}} \sin(2\pi n/N_{\text{cycle}})$ . In this study, we set a period of the simulation steps per cycle to  $N_{\text{cycle}} = 10^4$  which is sufficiently large.

### III. RESULTS

#### A. Dynamics and Phase Diagram

First, we introduce the averaged particle displacements for one cycle defined by

$$\Delta r(t, T) = \frac{1}{N} \sum_{j=1}^N |\mathbf{r}_j(t+T) - \mathbf{r}_j(t)|. \quad (3)$$

This characterizes the reversibility of the particle trajectories and is often used as an order parameter of the RI transition.  $\Delta r(t, T) \sim 0$  if the system is in the reversible state and it is finite in the irreversible state. We regard the system is in the reversible state when  $\Delta r(t, T) < 10^{-6}$ . We measure  $\Delta r(t, T)$  for various values of both  $\varphi$  and  $\gamma_0$ . To cover the broad range of the parameter space of  $(\varphi, \gamma_0)$  efficiently, we use the finite frequency protocol with a large  $T$ . This protocol is much faster than that of the AQS. As we discuss below, the frequency dependence of  $\Delta r(t, T)$ , and thus the phase diagram, is weak as far as  $T$  is large enough. We switch to the AQS protocol when we compute the geometrical and mechanical properties because they sensitively depend on the frequency. In Figure 1, we show typical

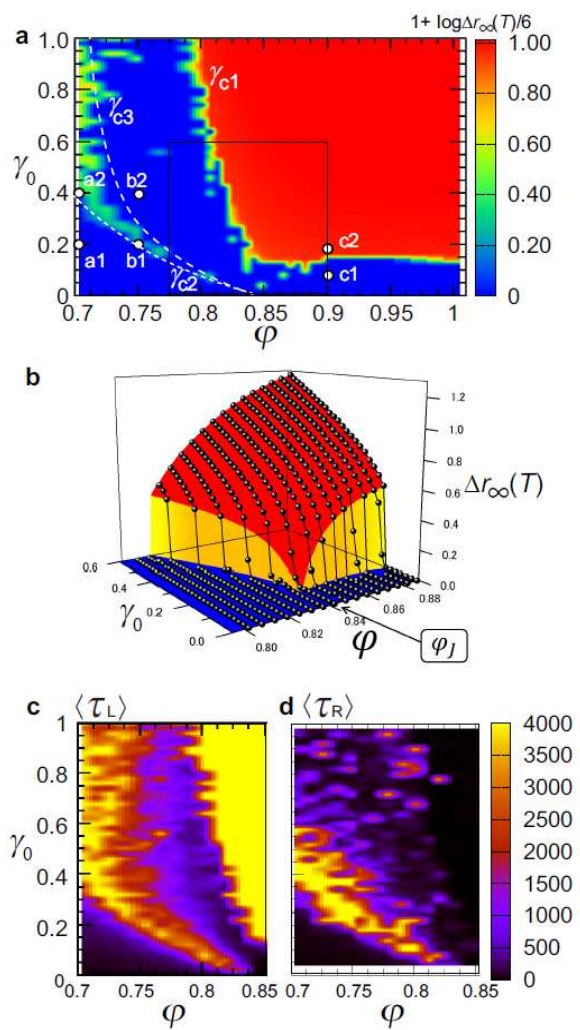


FIG. 2. The phase diagrams of the RI transition shown as the color map of several observables. (a): The phase diagram obtained from  $\Delta r_\infty(T)$  in the steady state. The color field presents the value of  $1 + \log \Delta r_\infty(T)/6$  (see the color bar).  $\gamma_{c1}$  (discontinuous),  $\gamma_{c2}$  (continuous), and  $\gamma_{c3}$  (discontinuous) indicate the locations of the phase boundaries (see the main text for detail). The two dashed lines,  $\gamma_{c2}$  (lower bound) and  $\gamma_{c3}$  (upper bound), are guides to the eye. (b): Bird's-eye view of  $\Delta r_\infty(T)$  as a function of  $\varphi$  and  $\gamma_0$  for the region marked by a black square in (a). The colored areas are the guide to the eye. (c): The phase diagram drawn using the averaged lifetime of irreversible trajectories  $\langle \tau_L \rangle$ . (d): The averaged relaxation time  $\langle \tau_R \rangle$ . For (c) and (d), the region above  $\varphi > 0.85$  is not shown because it is basically identical with those of (a).

time evolutions of  $\Delta r(t, T)$  for four representative densities below and above  $\varphi_J$  and for several  $\gamma_0$ 's. Figure 1a is the results at a low density,  $\varphi = 0.703$ , far below  $\varphi_J$ . For  $\gamma_0 \lesssim 0.40$ , the displacements exponentially relax to zero. As  $\gamma_0$  increases, the relaxation slows down, developing power-law tails, and eventually the system enters the irreversible state with finite  $\Delta r(t, T)$ 's. The result for a high density,  $\varphi = 0.901$ , far above  $\varphi_J$  is shown in

Figure 1b. Relaxation behavior is qualitatively different from that at low densities.  $\Delta r(t, T)$  starts from the irreversible (active) state with a finite value. It remains almost constant until it *discontinuously* drops to zero or enters to the reversible (absorbing) state. The heights of the plateau of  $\Delta r(t, T)$  are insensitive to  $\gamma_0$  but the relaxation time in the irreversible state increases sharply as  $\gamma_0$  increases before it eventually exceeds the time window of our simulation at  $\gamma_c \approx 0.14$ . The previous study has shown that  $\gamma_c$  where the relaxation time diverges matches with the yielding transition point  $\gamma_Y$  at which the system loses the elasticity and starts flowing [21]. We observed, at high densities, that a fraction of trajectories are multi-period reversible. In other words, some particles come back to their original positions only after several cycles. In the present study, we do not include the data for the analysis.

The results for intermediate densities between the low and high densities are surprisingly rich. Figure 1c shows the results at  $\varphi = 0.750$ . If  $\gamma_0$  is small, the relaxation behavior of  $\Delta r(t, T)$  is qualitatively the same as those at  $\varphi = 0.703$  and it decays exponentially. As  $\gamma_0$  increases,  $\Delta r(t, T)$  starts developing the power law tails. The relaxation time increases and eventually becomes larger than the simulation windows. As  $\gamma_0$  increases further, however, this trend is reversed and the relaxation time becomes shorter. In other words, the system shows the reentrant behavior. After this reentrance, the relaxation behavior qualitatively changes and becomes more like that observed above  $\varphi_J$  (Fig. 1b); it first quickly decays to a plateau, stay there for a long time, and then abruptly and discontinuously drop to zero. Contrary to the results at  $\varphi > \varphi_J$ , the heights of the plateau increase continuously and the relaxation time shortens as  $\gamma_0$  increases. This reentrant transition of the relaxation time below  $\varphi_J$  is already reported by Schreck *et al.* [12]. They found that this transition separates the two qualitatively different reversible phase which is referred to as the point-reversible and loop-reversible phases. We shall analyze thoroughly the dynamical and geometrical properties of these phases in the next subsection.

Figure 1d is the result at  $\varphi = 0.831$ , slightly below  $\varphi_J$ . In this region, we again observe the exponential relaxation of  $\Delta r(r, T)$  at very small  $\gamma_0$  ( $= 0.1$ ). As  $\gamma_0$  increased, however, the relaxation time barely increase but instead it develops the plateau with the finite heights and its behavior becomes more like that observed above  $\varphi_J$  (see Fig. 1a), *i.e.*, a quick decay to a plateau and sudden and step-wise relaxation to zero. For  $\gamma_0 \gtrsim 0.3$ ,  $\Delta r(t, T)$  remains constant in our simulation windows, suggesting that the system entered the irreversible state. It is interesting to observe a qualitatively similar behavior to that above  $\varphi_J$  even in the unjammed phase. In the next subsection, we show that the RI transition observed in this density regime is closely related to the macroscopic rheology.

Using these simulation results, we draw the *dynamical phase diagram* of the RI transition using  $\Delta r(t, T)$  in the

stationary state as the order parameter for a broad range of  $\varphi$  and  $\gamma_0$ . We run the long simulations up to  $t = 4000T$  and judge that the system is in the stationary state if  $\Delta r(t, T)$  becomes independent of time. We denote the ensemble average of  $\Delta r(t = 4000T, T)$  as  $\Delta r_\infty(T)$ . Note that the diffusion constant  $D$  is an alternative candidate of the order parameter. In Ref. [21], it is shown that the position of the RI transition is not affected by choice of the order parameters if the period-doubling data are excluded. Figure 2a is the phase diagram drawn as the contour plot of  $\Delta r_\infty(T)$  as a function of  $(\varphi, \gamma_0)$ . In order to enhance the visibility of the small values of  $\Delta r_\infty(T)$ ,  $1 + \log \Delta r_\infty(T)/6$  is used to define the color map. The reversible region where  $\Delta r_\infty(T) = 0$  (or more precisely  $\Delta r_\infty(T) < 10^{-6}$ ) is colored by blue and the largest value of  $\Delta r_\infty(T) = 1$  is colored by red (see the color column). In order to draw this figure, we simulated the system for the range of  $0.7 \leq \varphi \leq 1.0$  and  $0 \leq \gamma_0 \leq 1.0$  for grid points separated by  $\delta\varphi = 0.05$  and  $\delta\gamma_0 = 0.05$  for most cases. The finer grid sizes of  $\delta\varphi = 0.01$  and  $\delta\gamma_0 = 0.02$  are used in the vicinity of the phase boundaries. This phase diagram reflects the dynamic properties of  $\Delta r(t, T)$  observed in Fig. 1. There are several qualitative features which draw our attention.

Firstly, in the high-density side above  $\varphi \gtrsim 0.8$ , one observes an irreversible phase colored by red which is sharply separated from the reversible phase in blue.  $\gamma_{c1}$  represents the phase boundary line. Above  $\varphi_J \approx 0.842$ , the irreversible phase is always observed and the transition point  $\gamma_{c1} \approx 0.15$  is almost constant over all densities above  $\varphi_J$ . The abrupt change of the colors at  $\gamma_{c1}$  is a consequence of a sudden and discontinuous increase of  $\Delta r_\infty(T)$  [21]. The value of  $\Delta r_\infty(T)$  in the irreversible phase is very close to 1 irrespective of  $\varphi$  and  $\gamma$ .  $\gamma_{c1}$  is not exactly constant. As  $\varphi$  is decreased from above, it is slightly bent upward around  $\varphi \approx 0.9$  and then downward as  $\varphi_J$  is approached, before it turns upward sharply at the edge at  $\varphi = \varphi_J$ .  $\gamma_{c1}$  increases sharply at  $\varphi < \varphi_J$ . The presence of the discontinuous transition below  $\varphi_J$  is also observed in Ref. [12]. In the large  $\gamma_0$  limit, this RI transition line seems to diverge at  $\varphi \approx 0.8$ . Note that this value is very close to the random loose packing density where the particles would undergo the mechanical transition if there is an interparticle frictional force. This result is reminiscent of the finding that configurations of the sheared frictionless spheres are similar to those of the shear jammed system of the frictional spheres reported in Ref. [25].  $\Delta r_\infty(T)$  at  $\varphi < \varphi_J$ , however, is quantitatively different. Its magnitude is not an order of unity but decreases as the density is decreased towards the phase boundary for a fixed  $\gamma_0$ . Figure 2b is the birds eye's view of  $\Delta r_\infty(T)$  near  $\varphi_J$ . It shows that the RI transitions of both sides of  $\varphi_J$  are discontinuous but  $\Delta r_\infty(T)$  tends to vanish at the  $\varphi = \varphi_J$ , while  $\gamma_{c1}$  there remains unchanged. It is premature to conclude that this vanishing order parameter is the sign of the continuous transition. It is because the resolution of the parameters is too low and assessing the critical behavior of  $\Delta r_\infty(T)$  at  $\varphi_J$  exactly is

challenging due to a subtle interplay of the criticalities of the jamming and RI transitions [23, 24]. We shall revisit this issue in future work.

Secondly, and most noticeably, there is a ‘‘peninsula’’ of the irreversible phase below  $\varphi_J$ , where  $\Delta r_\infty(T)$  is finite in the low-density and small- $\gamma_0$  region, surrounded by the reversible states. The presence of this irreversible region is a manifestation of the reentrant behavior of  $\Delta r(t, T)$  shown in Fig. 1b. As we shall discuss more in detail in the next subsection, this region is surrounded by the two phase boundaries on the low  $\gamma_0$ -side (denoted as  $\gamma_{c2}$ ) and upper  $\gamma_0$ -side (denoted as  $\gamma_{c3}$ ). We find that the RI transition across  $\gamma_{c2}$  is continuous whereas it is discontinuous at  $\gamma_{c3}$ . As the density increases, the two phase boundaries of  $\gamma_{c2}$  and  $\gamma_{c3}$  tend to converge to zero around  $\varphi_J$ . The phase boundaries of the irreversible phase, especially  $\gamma_{c3}$ , is jerky and blurred due to very large sample-to-sample fluctuations of  $\Delta r_\infty(T)$ . One may be tempted to consider this irreversible peninsula is a metastable state which vanishes in the large time limit ( $t \rightarrow \infty$ ) or in the AQS limit ( $T \rightarrow \infty$ ). However, we verify that this phase is unexpectedly stable and the dynamical behaviors of the particle trajectories in this phase are distinct from that outside of the irreversible phase. We also verify that this phase survives in the AQS limit.

Instead of the order parameter  $\Delta r_\infty(T)$ , one can employ the relevant time scales as the order parameters to draw the phase diagram. The phase boundaries are drawn as the points at which the time scales diverge. Note that there are two types of time scales in our systems depending on the nature of the RI transitions. If the transition is continuous as we observe at low densities,  $\Delta r_\infty(T)$  is well described by an exponential function from which one can define the relaxation time  $\tau_R$ . To define  $\tau_R$ , we use an empirical function given by [4]

$$\Delta r(t, T) = \Delta r_0 \frac{e^{-t/\tau_R}}{t^\delta}, \quad (4)$$

where  $\Delta r_0 \equiv \Delta r(t = 0, T)$ . On the other hand, if the transition is discontinuous as we observe at  $\gamma_{c1}$  and  $\gamma_{c3}$  in Fig. 2a,  $\Delta r_\infty(T)$  develops a plateau. There are initial relaxations towards the plateau and the final abrupt drops from the plateau to the reversible phase. We refer the time scale of the latter process as the life time  $\tau_L$  in order to discriminate the relaxation time  $\tau_R$  of the initial relaxation.  $\tau_R$  is obtained by fitting by the generalized expression of Eq. (4) given by

$$\Delta r(t, T) = (\Delta r_0 - \Delta r_s) \frac{e^{-t/\tau_R}}{t^\delta} + \Delta r_s, \quad (5)$$

where  $\Delta r_s$  is the plateau value. On the other hand, we define the life time  $\tau_L$  as the time at which  $\Delta r(\tau_L, T)$  drops to  $10^{-6}$ . Figure 2c and d are the phase diagram or the contour plots of the averaged values of  $\tau_L$  and  $\tau_R$ . The region above  $\varphi_J$  is not shown because it is identical to that for  $\Delta r_\infty(T)$ . In the vicinity of the phase boundary  $\gamma_{c2}$ , the iso- $\tau_L$  line coincides with the iso- $\tau_R$

line, since  $\Delta r_\infty$  continuously decreases to 0 toward the critical point. On the other hand, near  $\gamma_{c3}$ , the two time scales are decoupled. While the region where  $\tau_L > 4000T$  (yellow colored region in Fig. 2c) matches with the irreversible peninsula in Fig. 2a, The large  $\tau_R$  ridge only exists along  $\gamma_{c2}$ -line (see Fig. 2d). This result bolsters that the phase boundaries of the peninsula of the irreversible phase is delineated by the continuous transition at small  $\gamma_0$ 's and discontinuous transition at large  $\gamma_0$ 's. Schreck *et al.* [12] have demonstrated that this diverging time scale separates the reversible phase into the two distinct phases; the point-reversible phase where the one-cycle trajectory is completely affine-like and the loop-reversible phase where it is not. Our results suggest that there exist a (meta-)stable irreversible phase between the point- and loop-reversible phase. In the next subsection, we characterize this distinct phase using the topology of the one-cycle trajectories and their long time dynamics.

## B. Particle trajectories

The presence of the region of the large relaxation time in Fig. 1a is hardly the evidence that this peninsula is the *bona fide* irreversible phase. To identify the nature of this exotic state, we characterize the microscopic trajectories of particles inside and the vicinity of the peninsula in more detail. We analyze the microscopic trajectories of particles in several representative state points in the phase diagrams. Figures 3a1-c2 are the trajectories of a single particle for multiple cycles for the state points marked in Figure 1a. We plot the non-affine trajectories,  $\mathbf{r}_j^{(\text{NA})}(t) \equiv (x_j(t) - \gamma(t)y_j(t), y_j(t))$ , where the affine part of the displacement subtracted from the coordinate. Here, we used the finite frequency protocol with  $T = 10^4$ . We have also carried out the same analysis using the AQS protocol ( $T = \infty$ ) and found that the results do not qualitatively change. Dots which are connected by lines in each figure represent the position of the particle at each incremental step of strain for  $T/100$ .

If both  $\varphi$  and  $\gamma_0$  are very small, the trajectory is just a single point as shown in Fig. 3a1 because the particle is convected by the shear and, after a cycle, comes back to the original position without a collision with other particles. This reversible state is referred to as the point-reversible state [12]. This single point state is observed over the region where  $\varphi < \varphi_J$  and  $\gamma < \gamma_{c2}$ .

For  $\varphi > \varphi_J$ , on the other hand, the trajectories of the reversible phase are qualitatively different from the point-reversible trajectories, as shown in Figure 3c1. Each particle travels complicated non-affine trajectories until it comes back to the original position after one cycle. This is called the loop-reversible state. If  $\gamma_0$  is increased above  $\gamma_{c1}$  at a fixed  $\varphi (> \varphi_J)$ , the trajectory fails to close the loop after a cycle and the system becomes irreversible as demonstrated by previous studies [21]. We call this state the loop-irreversible (Fig. 3c2). This RI transition point coincides with the yielding transition ( $\gamma_c = \gamma_Y$ ) [20,

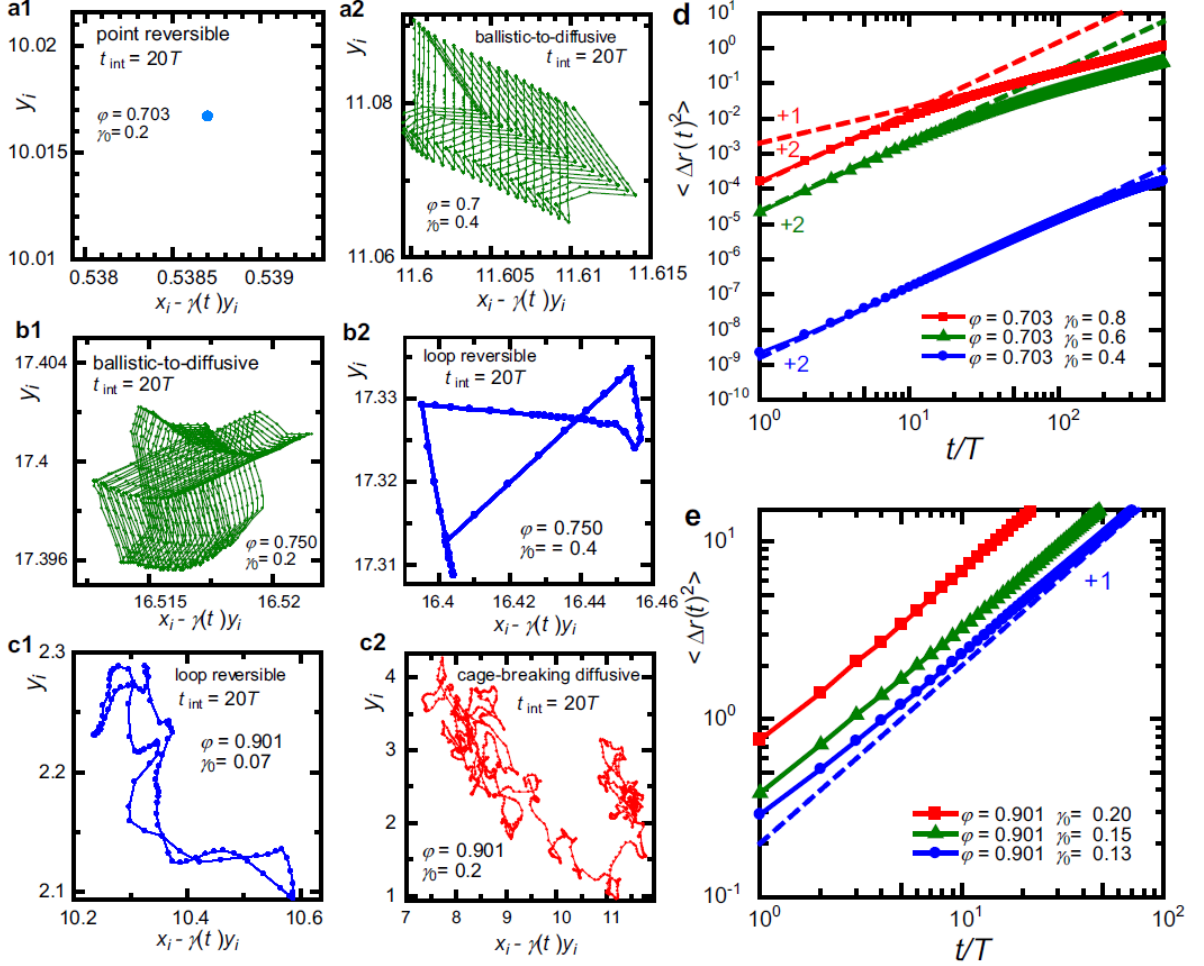


FIG. 3. (a1)–(c2): Representative particle trajectories during 20 cycles. The symbols a1–c2 corresponds to those marked in Fig. 1a. Depending on  $\gamma_0$  and  $\varphi$ , the topology of trajectories qualitatively change. (a1): A point reversible trajectories. (a2) and (b1): Ballistic-diffusive trajectories. (b2) and (c1): Loop-reversible trajectories. (c2): Cage-breaking diffusion. The mean squared displacements (d) at a small density,  $\varphi = 0.703$ , with  $\gamma_0 = 0.4, 0.6, 0.8$  and (e) at a high density  $\varphi = 0.901$  with  $\gamma_0 = 0.13, 0.15, 0.20$ .

21]. As  $\varphi$  is approached to  $\varphi_J$  from above, the trajectories become more complicated and some particles come back to the original positions only after several cycles [23]. The particle trajectories below and above  $\gamma_{c1}$  below  $\varphi_J$ , where the yielding transition is absent, are qualitatively the same as those above  $\varphi_J$ .

Striking are the behaviors of the trajectories at  $\varphi < \varphi_J$  and  $\gamma_0 > \gamma_{c2}$ . In the reversible phase above the peninsula, *i.e.*,  $\gamma_0 > \gamma_{c3}$ , the trajectories are again the loop-shaped but their shape is somewhat simpler than those observed at  $\varphi > \varphi_J$ . Figure 3b2 is the typical loop trajectory observed at  $\varphi = 0.75$  and  $\gamma_0 = 0.4$  which lies in the reversible phase well above  $\gamma_{c3}$ . We observed a variety of loop trajectories in this reversible phase, whose shapes vary depending on the locations in the parameter space. Inside the peninsula of the irreversible phase surrounded between  $\gamma_{c2}$  and  $\gamma_{c3}$ , the trajectories are very different. Figures 3a2 and b1) are the representative trajectories which are observed in this irreversible phase. The par-

ticles' trajectories in these figures are recorded over 20 cycles. The particles trace loop-like trajectories in each cycle but, at the very end of one cycle, they always fail to close the loop. After every cycle, the endpoints migrate by a very small distance and they depart from the original position. After many cycles, the trajectories eventually becomes diffusive. This crossover of the particle dynamics from a quasi-reversible to diffusive is most clearly demonstrated by evaluating the mean squared displacements (MSDs) defined by

$$\langle \Delta r^2(t) \rangle = \frac{1}{N} \left\langle \sum_{j=1}^N \left\{ \mathbf{r}_j^{(\text{NA})}(t_0 + t) - \mathbf{r}_j^{(\text{NA})}(t_0) \right\}^2 \right\rangle, \quad (6)$$

where  $N$  is the total number of particles,  $\mathbf{r}_j^{(\text{NA})}(t)$  is the non-affine displacement of the  $j$ -th particles.  $t_0$  is chosen to be longer than  $\tau_R$ , so as to ensure the system is in the stationary state. Figures 3d and 3e are the

MSDs below and above  $\varphi_J$  for several  $\gamma_0$ , respectively. Note that  $\langle \Delta r^2(t) \rangle = 0$  if the system is in the reversible state, as we measure the trajectories in the stationary state. The MSD for  $\varphi > \varphi_J$  (Fig.re 3e) is subdiffusive at short times,  $\langle \Delta r^2(t) \rangle \propto t^\alpha$  with  $\alpha < 1$ , but after several cycles they become diffusive,  $\langle \Delta r^2(t) \rangle \propto t$ . This subdiffusive behavior is the reflection of the particles motion hindered by the multiple collisions with surrounding particles like in the supercooled liquids near the glass transition point. We call this motion *the cage-breaking* diffusion. On the other hand, Figure 3d is the MSD in the irreversible phase at  $\varphi < \varphi_J$  (in the peninsula). Although the MSD becomes diffusive eventually, the short time behavior is ballistic first, *i.e.*,  $\langle \Delta r^2(t) \rangle \propto t^2$  for a long time. We refer to this behavior as *ballistic diffusive*. This ballistic motion is a direct reflection of the small but systematic migration of the endpoints shown in the trajectory in Fig. 3a2 and 3b1. The crossover time from the ballistic to diffusive regime agrees well with  $\tau_R$  and, as  $\gamma_0$  is lowered to  $\gamma_{c2}$  from above, it becomes longer and eventually goes out from the simulation window. Again we emphasize that the qualitative behaviors of the trajectories are insensitive to the frequencies of the oscillation and is observed in the AQS protocol as well. Finally, to reassure that the irreversible peninsula state is robust insensitive to the protocol to prepare the system and the initial configuration of the particles, we prepared a configuration obtained in the loop-reversible states at large  $\gamma_0$ 's and then carried out the same simulations. We found that the shape of the trajectories remain qualitatively unchanged and  $\Delta r(t, T)$  are identical to those obtained from the random configurations. These results bolster that the irreversible state which we observed is the genuine stable irreversible phases characterized by the continuous transition from the point-reversible to irreversible phase and the discontinuous transition from the irreversible to loop-reversible phase, as  $\gamma_0$  is increased for a fixed  $\varphi$ . Such an exotic reentrant transition is a consequence of the emergence of the complex geometrical landscape. At the intermediate  $\varphi$ 's and large  $\gamma_0$ 's, there is a dynamical phase where the particles can find the way back to the original position after long sojourns in the valleys of the complex geometrical landscape and multiple collisions with surrounding particles. Many cycles of slow or quasi-static shear cycles can train the system and encode and memorize the information of the optimized pathways for the particles to stay in their stable configurations. However, if  $\gamma_0$  is not large enough, particles cannot trace the encoded pathways and complete the loop in one cycle and thus fail to come back to their original positions. In the next subsection, we consider the relationship of the properties of the phase diagram with the geometrical properties of the sheared configurations of the particles.

### C. Geometry of the Particle configurations

Since the system we study is athermal, any nonequilibrium transition of the trajectories must be related to the geometrical properties imprinted in the configuration of the particles. To characterize them, we evaluate the contact number  $Z$  of adjacent particles. In principle,  $Z$  can be obtained by integrating the radial distribution function  $g(r)$  over the distance of the first coordination shell. Contrary to the overall shape of the phase diagram and qualitative behaviors of the trajectories, the contact number is very sensitive to the frequency of the oscillatory shear. Therefore, we employ the AQS protocol to draw the iso- $Z$  lines. We use the method proposed by Vinutha *et al.* [25]. Even in the AQS protocols, the number of the strain step per cycle  $N_{\text{cycle}}$  is finite and, therefore, the aperture between the pair of particles at contact,  $r_{ij} - \sigma_{ij}$  where  $\sigma_{ij} \equiv (\sigma_i + \sigma_j)/2$ , is inevitably finite. To remove this unwanted effect and obtain the true contact number in the  $N_{\text{cycle}} = \infty$  limit, we introduce a small 'tolerant' inter-particle gap length,  $a_{\text{th}}$ . With this parameter, the contact number  $Z$  is reasonably estimated by

$$Z = \int_{a_{ij}}^{a_{ij} + a_{\text{th}}} 2\pi r g(r) dr. \quad (7)$$

We calculated  $Z$  as a function of  $a_{\text{th}}$  and assured that  $Z$  saturates and reaches a limiting value in the limit  $a_{\text{th}} \rightarrow 0$ . We fix  $a_{\text{th}}$  to be  $a_{ij}/N_{\text{cycle}}$  which is small enough for  $Z$  to stay in this limiting value [25].

In Figure 4a, the iso- $Z$  lines for several  $Z$ 's obtained using the above-mentioned method are superimposed on top of the phase diagram shown in Figure 2a. One first observes the isostatic line with  $Z = 4$  ( $= 2d$ ) running vertically at  $\varphi \approx \varphi_J$ , as it is expected from the Maxwell's stability criterion [31]. A small deviation of the intersection at  $\gamma_0 = 0$  from the true  $\varphi_J \approx 0.842$  is due to the small system size. The line with  $Z = 5$  is located at much higher density and run almost parallel with the isostatic line. The line with  $Z = 3$  starts slightly below  $\varphi_J$  at  $\gamma_0 = 0$  but bends toward lower  $\varphi$ 's as  $\gamma_0$  increases, and merges to the phase boundary of the discontinuous RI transition line  $\gamma_{c1}$  which eventually converges to  $\varphi \approx 0.80$ , the random loose packing density. This behavior is analogous to the finding for the three-dimensional system [25], in which the configurations obtained at  $Z = d + 1$  under shear are analogous to those of the jammed frictional particles. The line with  $Z = 2$  coincides with the iso- $\tau_L$  line with  $\tau_L = 1000T$  shown as the orange colored region in Fig. 2c. The line with  $Z = 1$  almost matches with the phase boundary  $\gamma_{c3}$  where the discontinuous and reentrant RI transition takes place. Finally, there is a region of  $Z = 0$  in small  $\varphi$  and  $\gamma_0$  region, where the system is in the point-reversible state. As  $\gamma_0$  is increased for a fixed  $\varphi$ , there is a point at which  $Z$  becomes finite. Interestingly, these points agree well with the phase boundary  $\gamma_{c2}$  where the continuous RI

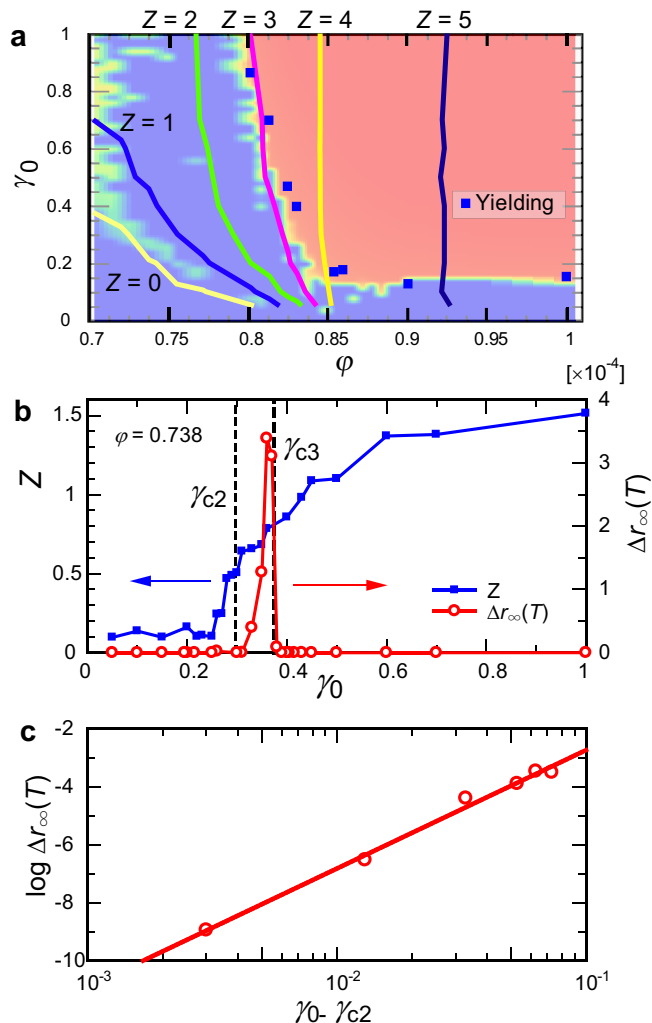


FIG. 4. (a): The iso- $Z$  lines superimposed on the phase diagram shown in Fig. 2a. They are obtained from the AQS protocol. Square dots are the yielding transition points obtained from the steady shear protocol. See Fig. 5 for more details. (b):  $\gamma_0$ -dependence of  $Z$  and  $\Delta r_\infty(T = \infty)$  at  $\varphi = 0.738$  obtained from the AQS protocol. (c): Replot of  $\Delta r_\infty(T = \infty)$  shown in Fig. 4b as a function of  $\gamma_0 - \gamma_{c2}$ . The solid line is the fit by  $\Delta r_\infty(T = \infty) = A(\gamma_0 - \gamma_{c2})^\beta$  with  $\beta = 4.1$  and  $\gamma_{c2} = 0.29$ .

transition takes place. The yellow line in Figure 4b represents the points at which  $Z$  exceeds 0.2.

In Figure 4b, we show the  $\gamma_0$ -dependence of both  $\Delta r_\infty(T = \infty)$  and  $Z$  at a fixed  $\varphi \approx 0.738$ . Here  $\Delta r_\infty(T = \infty)$  is evaluated using the AQS protocol and with much longer cycles of  $n = 40000$  than those used to draw Fig. 2a to exclude unwanted metastable samples. One observes that  $Z$  starts growing continuously from zero to finite values around the transition point  $\gamma_{c2}$  and reaches  $Z = 1$  in the vicinity of  $\gamma_{c3}$  where  $\Delta r_\infty(T = \infty)$  drops to zero discontinuously. This figure also shows clearly the continuous growth of  $\Delta r_\infty(T = \infty)$  at  $\gamma_{c2}$ . However, one realizes that its critical growth is

qualitatively different from those observed at very low densities where the RI transition is akin to those of the DP universality class [4]. Figure 4c shows  $\Delta r_\infty(T = \infty)$  as a function of the distance from RI transition point  $\gamma_0 - \gamma_{c2}$ . The result is well fitted by

$$\Delta r_\infty(T = \infty) = A(\gamma_0 - \gamma_{c2})^\beta \quad (8)$$

with an exponent  $\beta \approx 4.1$  and  $\gamma_{c2} \approx 0.29$ . This exponent is far larger than those of the conserved DP universality class, or Manna class,  $\beta_{DP} = 0.624 \pm 0.029$  [32]. The discrepancy from the Manna class is not surprising because the transition at this density is escorted by an encoded geometrical change manifested by the increasing contact number and it is qualitatively distinct from the DP transition where the configuration of the particles is completely random.

#### D. Yielding transition below $\varphi_J$

Lastly, let us focus on the  $\gamma_{c1}$ -line slightly below  $\varphi_J$ . At  $\varphi > \varphi_J$ ,  $\gamma_{c1}$  matches with the yielding transition line as a natural consequence that the elastic response of the system is associated with the reversible trajectories and the trajectories become diffusive in the plastic flow regime. It is somewhat surprising that the RI transition line still survives even below  $\varphi_J$  where the system is in the fluid phase and the yielding transition is completely absent if one uses the AQS protocol. As we demonstrated in the previous subsection,  $\gamma_{c1}$  below  $\varphi_J$  matches with the iso- $Z$  line with  $Z = 3$ . The presence of this RI transition slightly below  $\varphi_J$  is already reported by Schreck *et al.* [12] and Vinutha *et al.* have reported that the sheared frictionless particles below  $\varphi_J$  develop structural configurations with  $Z = d + 1$  which would stabilize the system mechanically if the friction force is turned on [25]. This implies that the information of the mechanical properties are embedded in the sheared configurations. Such a hidden mechanical information would be detected either by turning on the friction force between the particles or by observing the transient mechanical response with time dependent strain. We adopt the latter strategy, *i.e.*, we exert the shear strain with *finite* strain rate on the system. We use the simple unidirectional shear with a constant strain rate  $\dot{\gamma}$  and the particles are driven with Eq. (1). We measure the shear stress  $\sigma_{xy}$  defined by

$$\sigma_{xy} = \frac{1}{2L^2} \sum_{j,k} \frac{x_{jk}y_{jk}}{r_{jk}^2} \frac{\partial U}{\partial r_{jk}}. \quad (9)$$

Figure 5a is the strain ( $\gamma$ ) dependence of  $\sigma_{xy}$  at  $\dot{\gamma} = 10^{-5}$  for various  $\varphi$  below  $\varphi_J$ . The stress-strain curves are averaged over 1000 independent initial configurations which are generated by the AQS oscillatory shear simulations at  $\gamma_0 = 1.0$  for each packing fraction. These stress-strain curves demonstrate typical yielding behaviors from the elastic to the flowing phase;  $\sigma_{xy}$  grows linearly with  $\gamma$

and then yields at  $\gamma = \gamma_Y$  followed by the steady plastic flow regime where  $\sigma_{xy}$  is constant. Interestingly, the yielding transition point  $\gamma_Y$  increases when  $\varphi$  decreases and it matches with  $\gamma_{c1}$  as shown in Fig. 4a. This behavior is very similar to the that observed experimentally in athermal colloidal suspensions below the glass transition point [33].

One observes the elastic regime before the yielding transition. However, the close inspection reveals that the elastic response against  $\gamma$  is not linear. Figure 5b is the log-log plot of the stress-strain curve at very small  $\gamma$  for several  $\varphi$ 's, where the residual stress at  $\gamma = 0$  is excluded from  $\sigma_{xy}$ . We find that  $\sigma_{xy}$  follows the nonlinear behavior which is well fitted by

$$\sigma_{xy} \propto \sqrt{\gamma}. \quad (10)$$

This is reminiscent of the softening of the stress observed above  $\varphi_J$  [24, 34, 35]. In the studies above  $\varphi_J$ , the softening is observed after the linear elastic regime at even smaller  $\gamma$  but we did not observe the linear region. Figure 5b demonstrates that the softening region crosses over to the another nonlinear region with  $\sigma_{xy} \propto \gamma^a$  with a constant  $a \approx 1.3$ . This is again analogous with the findings reported above  $\varphi_J$  [24]. This crossover  $\gamma$  is very sensitive to  $\varphi$  and increases as  $\varphi_J - \varphi$  increases. This result suggests that the instability of the trajectories which controls the quasi-plastic event above  $\varphi_J$  also exists below  $\varphi_J$ .

Figure 5c is  $\sigma_{xy}$  for a fixed  $\varphi$  and for several  $\dot{\gamma}$ 's. It demonstrates that the amplitude of  $\sigma_{xy}$  is linear to  $\dot{\gamma}$ . All data are collapsed to a single line when scaled by a constant  $A$  proportional to  $\dot{\gamma}$ , which implies that  $\gamma_Y$  is insensitive to  $\dot{\gamma}$ . In Fig. 5d, we show the yield stress  $\sigma_Y \equiv \sigma_{xy}(\gamma = \gamma_Y)$  as a function of  $\varphi$  for several  $\dot{\gamma}$ . While the value above  $\varphi_J$  is insensitive to  $\dot{\gamma}$ ,  $\sigma_Y$  increases almost linearly with  $\dot{\gamma}$  below  $\varphi_J$ .

#### IV. SUMMARY AND CONCLUSIONS

To summarize, we numerically studied the reversible-irreversible (RI) transitions in particle trajectories for a wide range of densities below and above the jamming transition density  $\varphi_J$ . Particular emphasis is placed on the densities below  $\varphi_J$ , where we have observed very rich phases and mechanical behaviors.

Well below  $\varphi_J$ , there is a transition from the point-reversible to the irreversible phase when  $\gamma_0$  is increased for a fixed density before it enters the loop-reversible state at higher  $\gamma_0$ 's. The transition from the point-reversible to the irreversible phases is a continuous transition, whereas the irreversible to loop-reversible transition is discontinuous. Although the simulation windows are limited and it may sound difficult to judge whether they are the true nonequilibrium transitions or a transient crossover. However, the microscopic trajectories inside the irreversible region becomes diffusive after a very long ballistic initial growth. It is surprising to observe

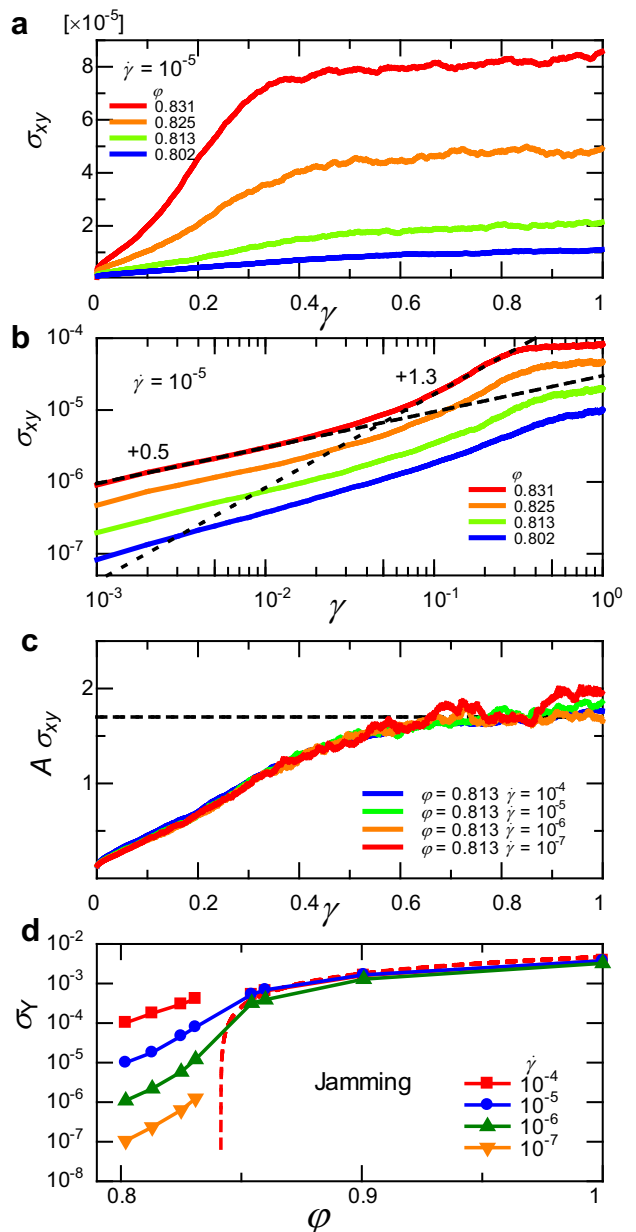


FIG. 5. (a):  $\gamma$ -dependence of the shear stress  $\sigma_{xy}$  for various  $\varphi$  at finite shear rate  $\dot{\gamma} = 10^{-5}$ . (b): The same as (a) but at small  $\gamma$ 's in the log-log plot. Dotted and broken lines are the fit with  $\gamma^{0.5}$  and  $\gamma$ , respectively. (c):  $\gamma$ -dependence of the scaled shear stress  $A\sigma_{xy}$  at  $\varphi = 0.813$ , where  $A$  is set to be  $A \sim \dot{\gamma}^{-1}$ . The dash line represents the steady state of  $\sigma_{xy}$  above shear yielding point  $\gamma_Y$ . (d):  $\varphi$  dependence of yield stress  $\sigma_Y$  for various  $\dot{\gamma}$ . The dash line represents  $\sigma_{xy} = C(\varphi - \varphi_J)$ , where  $C = 0.03$  and  $\varphi_J = 0.8425$ .

such reentrant transition because, for the particle trajectory to close a loop at the end of one or multiple cycle(s), a minimal amount of strain amplitude would be necessary for the particle to be driven along the pathway encoded in the complex geometrical landscape of the system.

The RI transition slightly below  $\varphi_J$  was also surprising. The transition is discontinuous as it is the case above  $\varphi_J$

but the order parameter  $\Delta r_\infty(T)$  is much smaller than that above  $\varphi_J$  and  $\gamma_c$  sharply increases as  $\varphi$  depart from  $\varphi_J$ . The system is completely stress-free, or  $\sigma_{xy} = 0$ , in the AQS limit and thus the yielding transition is absent. However, the mechanical properties are encoded in the sheared configurations of the particles even below  $\varphi_J$ . We found that the stress becomes finite and the yielding behaviors emerge as the strain rate  $\dot{\gamma}$  increases. The yielding transition points agree with the RI transition line irrespective of  $\dot{\gamma}$ . We also show the elastic response at small strains is highly nonlinear and proportional to  $\sqrt{\gamma}$  as it was recently found above  $\varphi_J$  [24, 34, 35]. This implies the jamming criticality which controls mechanical and rheological behaviors near  $\varphi_J$  survive below  $\varphi_J$ .

All these rich nonequilibrium behaviors are encoded in the geometrical properties of the configuration generated by shear. The contact number  $Z$  is a good measure and we found that the iso- $Z$  lines with different  $Z$  are placed on top of the phase boundaries of the RI transition below  $\varphi_J$ . The line at which  $Z$  becomes finite matches with the phase boundary between the point-reversible and irreversible phase ( $\gamma_{c2}$ ).  $Z = 1$  corresponds to  $\gamma_{c3}$  where the discontinuous transition from the irreversible to loop-reversible phase takes place. The line of  $Z = 2$  lies at the region where one observes the crossover of the dynamics of  $\langle \Delta r(t) \rangle$  from the two-step to single exponential relaxation. And the line of  $Z = 3$  matches with  $\gamma_{c1}$  at  $\varphi < \varphi_J$ , where the system would acquire the mechanical rigidity if the particles had the frictions [25]. We emphasize that the densities which we explored here are still large compared with the systems explored in Refs. [3–6] where the system is very dilute and the reversible trajectories are always affine-like, or point-reversible. In contrary, percolations of the sheared particles' configurations and the multiple collisions between particles are essential in the system we studied. Therefore, the continuous transition which is reported here is not a simple extrapolation of the RI phase transition line at the dilute limit and the nature of the RI transition is also very different. Indeed, the critical exponent for  $\Delta r$  at  $\gamma_{c2}$  (see Fig. 4c) is distinct from those predicted for the direct percolation theory and our system belongs to the different universality class.

The missing piece in this study is the nature of the RI transition just at  $\varphi_J$ , which we deliberately avoid

studying because the interplay of the jamming criticality and the RI transition makes the analysis of the trajectories very challenging [23]. We only reported the overall behavior of the order parameters such as  $\Delta r_\infty(T)$  (see Fig. 2b) which tends to vanish at  $\varphi_J$ . However, it is premature to conclude that this is the compelling evidence of the continuous transition because the resolution of the parameters is still low to zero in the critical regime and there is no sign of the relaxation time  $\tau_R$  (see Fig. 2d). This is the region where the intricate microscopic trajectories affect the nontrivial and nonlinear rheological response, especially like the softening observed in this study below  $\varphi_J$  and in the literatures above  $\varphi_J$  [24, 34, 35]. The studies in this direction are left for future work. Another interesting issue is the memory effects which recently attract much attentions in the context of the RI transitions in athermal particle systems [36–38]. It was revealed that “the memory” of particles' configurations can be encoded in the systems by a cyclic training but the nature of the imprinted memory in the high density amorphous solids [37] (in the loop-reversible phase) are very different from that for the dilutes systems (in the point-reversible phase). The diverse phase diagram shown in this paper hints that rich memory effects are observed even below the jamming transition point [39].

Finally, we remark that the rich dynamical transitions might not be limited to the athermal particles systems but should be generally observed in the hard condensed matter systems in which the RI transitions are observed [8, 9, 40, 41]. It would be interesting to study how the effect of the long-range interaction or the absence of the clear jamming point in these systems influence the observed phase diagrams.

## ACKNOWLEDGMENTS

We thank L. Berthier, S. Sastry, K. A. Takeuchi, H. Hayakawa, M. Otsuki, and E. Tjhung for valuable discussions. The research leading to these results has received funding from JSPS Kakenhi (No. 25000002, H16H04034, 15H06263, 16H04025, 16H06018, 18H01188, and 19K03767).

- 
- [1] H. Hinrichsen, *Adv. Phys.*, 2000, **49**, 815 .
  - [2] M. Henkel, H. Hinrichsen, and S. Lubeck, *“Nonequilibrium phase transitions I: Absorbing phase transitions”* (Springer Verlag, Heidelberg, 2008).
  - [3] D. J. Pine, J. P. Gollub, J. F. Brady, and A. M. Leshansky *Nature*, 2005, **438**, 997.
  - [4] L. Corté, P. M. Chaikin, J. P. Gollub, D. J. Pine, *Nat. Phys.*, 2008, **4**, 420.
  - [5] L. Milz and M. Schmiedeberg, *Phys. Rev. E*, 2013, **88**, 062308.
  - [6] E. Tjhung and L. Berthier, *Phys. Rev. Lett.*, 2015, **114**, 148301.
  - [7] K. A. Takeuchi, M. Kuroda, H. Chaté, and M. Sano, *Phys. Rev. Lett.*, 2007, **99**, 234503.
  - [8] S. Okuma, Y. Tsugawa, and A. Motohashi, *Phys. Rev. B*, 2011, **83**, 012503.
  - [9] B. L. Brown, C. Reichhardt, and C. J. O. Reichhardt, 2019, *New J. Phys.* 21, 013001.
  - [10] M. Sano and K. Tamai, *Nat. Phys.*, 2016, **12**, 249-253.
  - [11] M. Lundberg, K. Krishan, N. Xu, C. S. O’Hern, and M. Dennin, *Phys. Rev. E*, 2008, **77**, 041505.

- [12] C. F. Schreck, R. S. Hoy, M. D. Shattuck, and C. S. O'Hern, *Phys. Rev. E*, 2013, **88**, 052205.
- [13] I. Regev, T. Lookman, and C. Reichhardt, *Phys. Rev. E*, 2013, **88**, 062401.
- [14] D. Fiocco, G. Foffi, and S. Sastry, *Phys. Rev. E*, 2013, **88**, 020301(R).
- [15] N. C. Keim and P. E. Arratia, *Soft Matter*, 2013, **9**, 6222.
- [16] N. C. Keim and P. E. Arratia, *Phys. Rev. Lett.*, 2014, **112**, 028302.
- [17] K. H. Nagamanasa, S. Gokhale, A. K. Sood, and R. Ganapathy, *Phys. Rev. E*, 2014, **89**, 062308.
- [18] I. Regev, J. Weber, C. Reichhardt, K. A. Dahmen, and T. Lookman, *Nat. Comm.*, 2015, **6**, 8805.
- [19] N. V. Priezjev, *Phys. Rev. E*, 2013, **87**, 052302.
- [20] E. D. Knowlton, D. J. Pine, and L. Cipelletti, *Soft Matter*, 2014, **10**, 6931.
- [21] T. Kawasaki, and L. Berthier, *Phys. Rev. E*, 2016, **94**, 022615.
- [22] E. Tjhung and L. Berthier, *Phys. Rev. E*, 2017, **96**, 050601.
- [23] M. O. Lavrentovich, A. J. Liu, and S. R. Nagel, *Phys. Rev. E*, 2017, **96**, 020101.
- [24] S. Dagois-Bohy, E. Somfai, B. P. Tighe, and M. van Hecke, *Soft Matter*, 2017, **13**, 9036.
- [25] H. A. Vinutha and S. Sastry, *Nat. Phys.*, 2016, **12**, 578.
- [26] H. A. Vinutha and S. Sastry, *J. Stat. Mech.*, 2016, **2016**, 094002.
- [27] P. Das, H. A. Vinutha, and S. Sastry, arXiv:1907.08503.
- [28] E. Lerner, G. During, and M. Wyart, *Proc. Ntrl. Acad. Sci. U. S. A.*, 2012, **109** 4798.
- [29] D. J. Durian, *Phys. Rev. Lett.*, 1995, **75**, 4780.
- [30] M. Allen and D. Tildesley, *“Computer Simulation of Liquids”* (Oxford University Press, Oxford, 1987).
- [31] M. van. Hecke, *J. Phys.: Condens. Matter*, 2010, **22**, 033101.
- [32] S. Lubeck, *International Journal of Modern Physics B*, 2004, **18**, 3977.
- [33] T. G. Mason, J. Bibette, and D. A. Weitz, *J. Colloid Interface Sci.*, 1996, **179**, 439.
- [34] M. Otsuki and H. Hayakawa, *Phys. Rev. E*, 2014, **90**, 042202.
- [35] D. Nakayama, H. Yoshino, and F. Zamponi, *J. Stat. Mech.*, 2016, **2016**, 104001.
- [36] N. C. Keim and S. R. Nagel, 2011, *Phys. Rev. Lett.* **107**, 010603.
- [37] D. Fiocco, G. Foffi, and S. Sastry, *Phys. Rev. Lett.* 2014, **112**, 025702.
- [38] N. C. Keim, J. D. Paulsen, Z. Zeravcic, S. Sastry, and S. R. Nagel, *Rev. Mod. Phys.* 2019, **91**, 035002.
- [39] T. Kawasaki and K. Miyazaki, (in preparation)
- [40] N. Mangan, C. Reichhardt, and C. J. O. Reichhardt, *Phys. Rev. Lett.* 2008, 100, 187002.
- [41] M. Dobroka, Y. Kawamura, K. Ienaga, S. Kaneko and S. Okuma *New J. Phys.* 2017, **19** 053023.